Available online at www.sciencedirect.com

jmr&t Journal of Materials Research and Technology

www.jmrt.com.br

Original Article

Effects on hardness and microstructure of AISI 1020 low-carbon steel processed by high-pressure torsion☆

Diana Maritza Marulanda Cardona[a], *Jittraporn Wongsa-Ngam*[b], *Hernando Jimenez*[a], *Terence G. Langdon*[c,*]

[a] *Research Group in Energy and Materials (REM), Faculty of Mechanical Engineering, Universidad Antonio Nariño, Bogotá, Colombia*
[b] *Department of Mechanical Engineering, Faculty of Engineering, King Mongkut's Institute of Technology Ladkrabang, Bangkok, Thailand*
[c] *Materials Research Group, Faculty of Engineering and the Environment, University of Southampton, Southampton, United Kingdom*

ARTICLE INFO

Article history:
Received 10 April 2017
Accepted 8 May 2017
Available online 23 June 2017

Keywords:
1020 steel
High pressure torsion
Hardness

ABSTRACT

Low-carbon steel AISI 1020 was subjected to high-pressure torsion (HPT) with 6.0 GPa pressure through 1/4–5 turns. The microstructures of the samples in each turn were studied by means of X-ray diffraction (XRD) analyzing the changes in micro-strain, crystallite size and lattice parameter. Vickers testing was utilized to study the microhardness behavior of the samples subjected to HPT processing. The morphology evolution of the samples and especially the changes in ferrite and pearlite structures were studied for different numbers of turns using scanning electron microscopy (SEM).

1. Introduction

Low-carbon steel AISI 1020 is widely used as a construction material and for manufacturing of machine parts. Improving the mechanical and surface properties of this steel has been an important research field in materials science in the last decades because of its technological use. Usually, thermochemical heat treatments such as carbo-nitriding or boronizing have been used to improve the tribological behavior of AISI 1020 steel [1,2]. However, the use of severe plastic deformation (SPD) processes have shown important results in improving properties such as the hardness for this type of material [3].

High-pressure torsion (HPT) is a process that belongs to the SPD techniques. HPT is one of the most important and

☆ Paper was a contribution part of the 3rd Pan American Materials Congress, February 26th to March 2nd, 2017.

* *Corresponding author.*
E-mail: t.g.langdon@soton.ac.uk (T.G. Langdon).

http://dx.doi.org/10.1016/j.jmrt.2017.05.002

effective techniques for producing nanostructured and ultrafine-grained metals. In the HPT procedure, a disk-shaped sample is positioned between two anvils and then it is processed by applying simultaneously hydrostatic pressure and torsional straining, thereby modifying the internal structure of the material and achieving exceptional grain refinement even at the nanometer level. This processing also increases the hardness and leads to exceptionally high strength [4,5]. In this research, a low-carbon steel, AISI 1020, was subjected to HPT processing and the microstructural evolution, crystallographic behavior and changes in microhardness were studied.

2. Experimental materials and procedures

Cylindrical samples of 10 mm diameter and ~0.8 mm length of AISI 1020 steel were subjected to HPT processing. The samples were cut from a rod taken by machining from a block of AISI 1020 commercial steel. In order to relieve the stress introduced by machining, the samples were heated to 650 °C for 15 min. This thermal treatment introduced no change in the mechanical and structural properties of the samples.

The HPT process was performed at room temperature under quasi-constrained conditions [6]. The HPT equipment consisted of upper and lower massive anvils having central depressions with diameters of 10 mm and depths of 0.25 mm where the samples were placed. The rotation speed of the lower anvil was 1 rpm with a 6.0 GPa pressure. Two separate disks of the cylindrical samples were processed at $N = 1/4$, $N = 1$, $N = 2$ and $N = 5$ turns for measurements of microhardness and microstructural analysis [7,8].

Microstructural observations were carried out using scanning electron microscopy (SEM) in a JEOL model JSM 6490-LV. The disks were polished to have a mirror-like surface and then they were etched with nital solution. Images were taken at 10 kV near the sample edge positions at a distance of ~4 mm from the center of each disk. The microstructural behavior of the samples was studied by XRD diffraction using Panalytical equipment in a Bragg–Brentano geometry with Kα Cu radiation of wavelength $\lambda = 1.5406$ Å and with a step of 0.02° at 45 kV and 40 mA. An X'Pert HighScore computer program was used to index the diffraction patterns. The crystallographic analysis of the samples was performed by means of the Williamson–Hall model. In this model the full broadening of the diffraction profiles depends on three key factors; the crystallite size, the microstrain and the instrumental broadening [9,10] so that

$$\beta_f^2 = \beta_c^2 + \beta_s^2 + \beta_i^2 \tag{1}$$

Using the Scherrer equation, the crystallite size (β_c) and microstrain (β_s) contributions are given by, respectively,

$$\beta_c = \frac{K\lambda}{L\cos\theta} \tag{2}$$

$$\beta_s = \frac{4\xi\sin\theta}{\cos\theta} \tag{3}$$

where L is the volume average of the crystal thickness in the direction normal to the diffraction reflecting planes, ξ is associated with the microdeformation of the lattice and K is the Scherrer constant. In practice, $K = 0.94$ for full width at half maximum (FWHM) of spherical crystals with cubic symmetry and. β_i represents the instrumental broadening.

The lattice parameter was found using the Nelson-Riley function. From the Bragg law the lattice parameter for each peak reflection (hkl) may be calculated. Using the Nelson-Riley method, the lattice parameter corresponding to each peak was plotted against the Nelson-Riley function (NRF). The precise lattice parameter was taken from the intercept of the linear fit. The NRF function is given by [11,12]:

$$\mathrm{NRF} = \frac{1}{2}\left(\frac{\cos^2\theta}{\sin\theta} + \frac{\cos^2\theta}{\theta}\right) \tag{4}$$

The changes in the crystallographic orientation were analyzed by means of the orientation coefficient C_o. This coefficient quantifies the crystalline orientation degree in a particular crystallographic plane (hkl). The crystallographic orientation coefficient C_o is the relationship between the relative intensities of the most intense diffraction peaks and it is defined as [13]:

$$C_o = \frac{I_{(hkl)}/I_0}{\frac{1}{n}\sum_n^1\left(\frac{I_{(hkl)}}{I_0}\right)} \tag{5}$$

where $I_{(hkl)}$ is the largest relative intensity of the peaks of orientation (hkl), I_0 is the powder pattern sample intensity (taken from the X'Pert HighScore program with reference code: 01-087-0721) and n is the number of peaks.

The microhardness measurements were taken using an Esseway model 600 hardness tester at a load of 50 g-F and 25 s dwell time. In the preparation of the samples for the hardness measurements, the samples were encapsulated in epoxy resin and then they were polished to have a mirror-like surface. The measurements were taken at positions separated by 30 μm across the diameters of each disk, and each selected point is the result of four individual measurements taken around this position and separated by 15 μm from each other to form a square. Color maps of the hardness variation were plotted over the entire surface of the sample. The construction of these maps was performed by replicating 8 parallel lines uniformly distributed to cover the entire surface of the sample.

3. Results and discussion

Fig. 1 shows the XRD patterns of the samples of AISI 1020 steel processed by HPT. Typical α-Fe XRD patterns with reflections in the crystallographic planes (110), (200) and (211) are observed. The crystallographic orientation was analyzed for each sample using the orientation coefficient C_o which is shown in Fig. 2. The samples have a strong preferred orientation in the plane (110) and this orientation is accentuated when the HPT processing is performed.

The relative intensities of the peaks corresponding to the crystallographic planes (200) and (220) decrease with

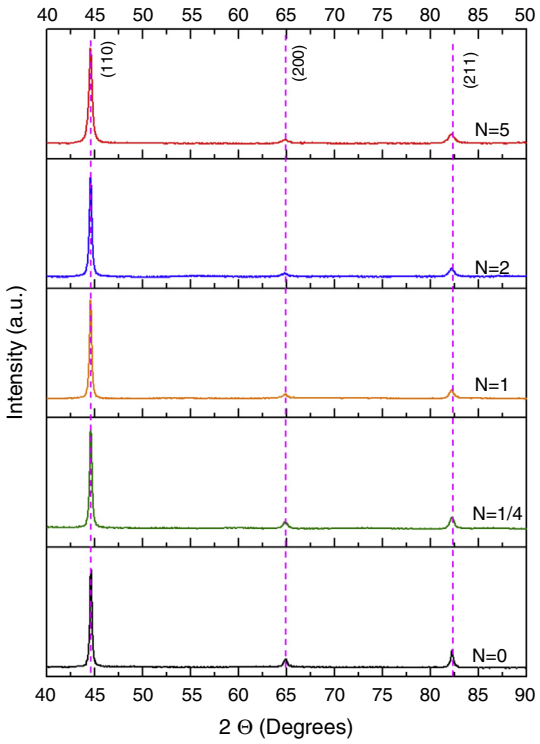

Fig. 1 – XRD patterns of AISI 1020 steel samples processed by HPT.

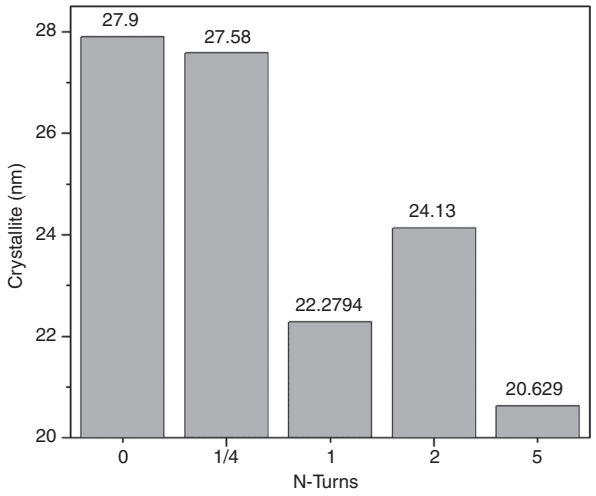

Fig. 3 – Crystallite size changes after HPT processing.

the numbers of turns. This indicates that the HPT process induces the occurrence of microstructural changes probably due to the formation of nanostructures and the dissolution of the pearlite lamella in the steel [14]. The lattice parameter calculated for the samples had an average value of 2.87 Å and this agrees with the lattice parameter reported for the reference pattern of X'Pert HighScore card (code: 01-087-0721). This parameter does not show significant variations with respect to the numbers of turns in the HPT process.

Fig. 3 shows the changes in crystallite size as a function of the numbers of turns. A decrease in crystallite size after the HPT process was evident, and this implies that after the HPT processing the crystal structure refinement of the steel is produced. On the other hand, an increase in the microstrain of the samples during HPT processing is observed as shown in Fig. 4.

Fig. 5 shows SEM images of the surfaces of the samples for each rotation. The images were taken near to the sample edges where high changes in the microstructure of the material are produced. The sample subjected to 1/4 turn shows a typical steel structure where perlite and ferrite features can be identified without a noticeable microstructural deformation. After 1, 2 and 5 turns, the deformation of the steel microstructure is clear; and ferrite and pearlite are present with elongated grain shapes. The microstructural refinement is observed by decreasing the initial interlamellar distance and the original grain size is compressed as more torsion is applied. This

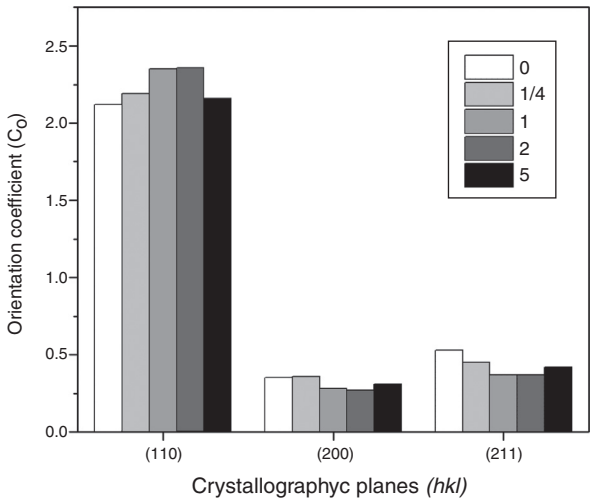

Fig. 2 – Orientation coefficient C_o of 1020 steel subjected to HPT processing.

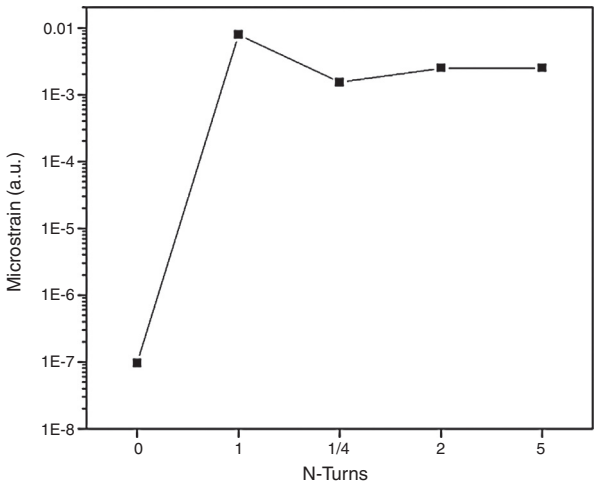

Fig. 4 – Microstrain evolution of 1020 steel samples after HPT processing.

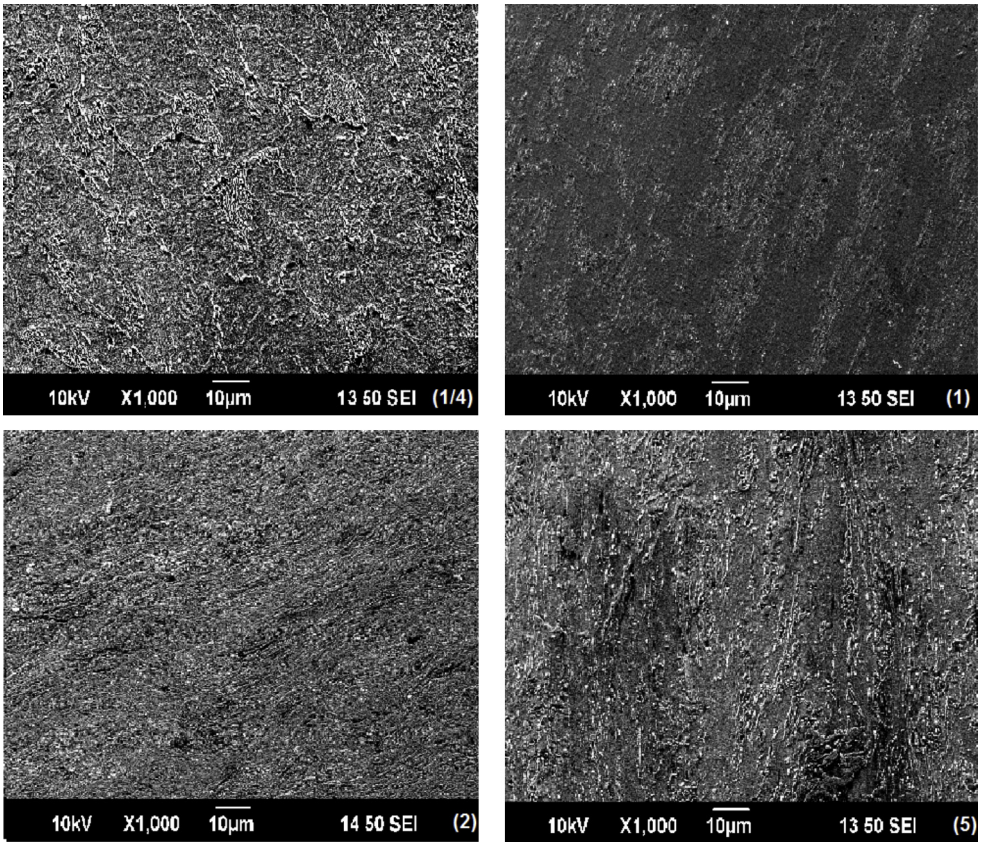

Fig. 5 – SEM images of the samples taken at ~4 mm of the mid-radius positions after HPT processing through different numbers of turns.

explains the increase in the microstrain and the reduction in the crystallite size registered by XRD (Figs. 3 and 4). This behavior was also reported by Ivanisenko et al. [15] and Kim et al. [16].

Changes in the microhardness along the diameter lines of the samples after HPT processing for different numbers of rotations are shown in Fig. 6. The hardness of the AISI 1020 steel before HPT processing was labeled with $N = 0$, with an average value of $\sim 174 \pm 8$ Hv, which is comparable with the hardness values reported for this commercial material. Fig. 5 shows the hardness distribution along the diametric lines of the samples processed by HPT at 1/4, 1, 2 and 5 turns, by comparison with the hardness obtained for the sample before HPT. After HPT processing, the hardness increased in all samples. The hardness was lower in the central region of the samples and was higher for measurements taken at the edge. Table 1 shows the hardness in the center region and outer region for each sample. The hardness distribution showed an inhomogeneous behavior and indicated that the microhardness had not attained the saturation condition. In order to achieve this condition, in which there are no mechanical properties or microstructural changes, it is necessary to apply a pressure larger than 6.0 GPa and/or increase the numbers of turns [15,17].

Table 1 – Hardness changes in the center and outer region.

# of turns	Center hardness	Outer hardness
0	174 ± 8	182 ± 8
1/4	233 ± 8	367 ± 9
1	274 ± 2	428 ± 6
2	360 ± 5	516 ± 5
5	306 ± 6	513 ± 5

Fig. 7 shows the 3D color-coded contour map of the hardness distribution over the entire surface of the sample processed to 1/4 turn. The projection of the contour in a 3D color map makes it possible to determine the distribution of hardness over the sample surface from the low hardness in a blue color to the highest values of hardness represented in a red color. This image establishes a quasi-symmetric behavior of the hardness around the center point of the sample and this agrees with predictions made by computational simulation models [18] using axisymmetric finite element formulation, as well as by experimental results reported for two separate commercial metal disks of Al-1050 and ZK60A through conventional HPT processing [18,19].

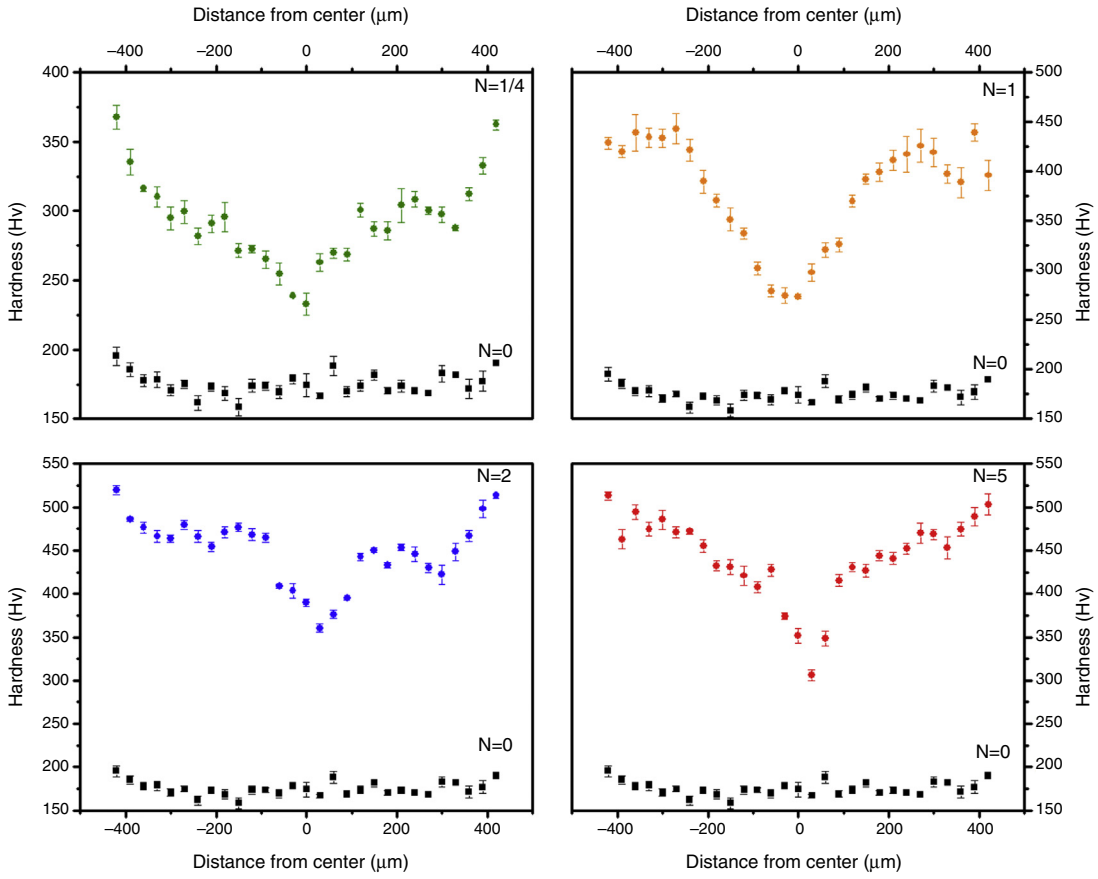

Fig. 6 – Microhardness profiles after processing through different numbers of turns: after 1/4 turn, after 1 turn, after 2 turns and after 5 turns.

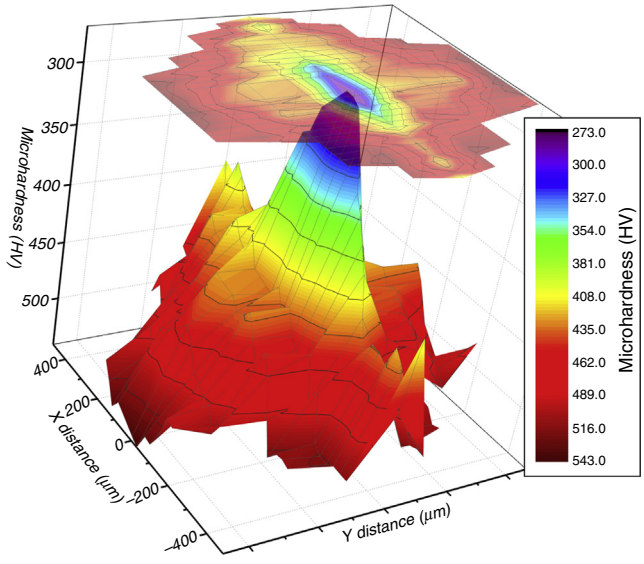

Fig. 7 – 3D color-coded contour maps of the hardness distributions for AISI 1020 after HPT processing for 1/4 turn.

4. Summary and conclusions

- AISI 1020 steel cylindrical samples were processed by high-pressure torsion (HPT) under a pressure of 6.0 GPa and the microstructure and microhardness were recorded after processing through 1/4–5 turns.
- The crystallite size and microstrain showed marked changes after the HPT processing.
- The hardness distribution indicated that full homogeneity of the microstructure was not reached and saturation would require applying pressures higher than 6.0 GPa and/or torsional straining through more than 5 turns.

Conflicts of interest

The authors declare no conflicts of interest.

Acknowledgments

The authors acknowledge the Universidad Antonio Nariño for financial support of the research project “Mechanical properties and electrochemical behavior of AISI 8620 steel processed using severe plastic deformation techniques”. This

work was also supported by the European Research Council under ERC Grant Agreement No. 267464-SPDMETALS.

REFERENCES

[1] Selçuk B, Ipek R, Karamış MB. A study on friction and wear behaviour of carburized, carbonitrided and borided AISI 1020 and 5115 steels. J Mater Process Technol 2003;141(October (2)):189–96.

[2] Sema PWT, Idem R, Liang Z, Tontiwachwuthikul P. Effects of flue gas composition on carbon steel (1020) corrosion in MEA-based CO_2 capture process. Int J Greenh Gas Control 2013;19(November):340–9.

[3] Rogachev SO, Sundeev RV, Khatkevich VM. Evolution of the structure and strength of steel/vanadium alloy/steel hybrid material during severe plastic deformation. Mater Lett 2016;173(June):123–6.

[4] Révész Á, Gajdics M, Schafler E, Calizzi M, Pasquini L. Dehydrogenation–hydrogenation characteristics of nanocrystalline Mg_2Ni powders compacted by high-pressure torsion. J Alloys Compd 2017;702(April):84–91.

[5] Eskandarzade M, Masoumi A, Faraji G, Mohammadpour M, Yan XS. A new designed incremental high pressure torsion process for producing long nanostructured rod samples. J Alloys Compd 2017;695(February):1539–46.

[6] Figueiredo RB, Cetlin PR, Langdon TG. Using finite element modeling to examine the flow processes in quasi-constrained high-pressure torsion. Mater Sci Eng A 2011;528:8198–204.

[7] Figueiredo RB, Pereira PHR, Aguilar MTP, Cetlin PR, Langdon TG. Using finite element modeling to examine the temperature distribution in quasi-constrained high-pressure torsion. Acta Mater 2012;60:3190–8.

[8] Wongsa-Ngam J, Kawasaki M, Zhao Y, Langdon TG. Microstructure evolution and mechanical properties of a Cu–Zr alloy processed by high-pressure torsion. Mater Sci Eng A 2011;528:7715–22.

[9] Khorsand Zak A, Abd. Majid WH, Abrishami ME, Yousefi R. X-ray analysis of ZnO nanoparticles by Williamson–Hall and size–strain plot methods. Solid State Sci 2011;13:251–6.

[10] Mote VD, Purushotham Y, Dole BN. Williamson–Hall analysis in estimation of lattice strain in nanometer-sized ZnO particles. J Theor Appl Phys 2012;6(December):6.

[11] Loghman-Estarki MR, Davar F, Ghorbani S, Zendehdel M, Taherian MH. Synthesis and characterization of aluminum oxy nitride (AlON) from the nanosized gel precursor. Ceram Int 2016;42(November):16861–6.

[12] Baykal A, Esir S, Demir A, Güner S. Magnetic and optical properties of $Cu_{1-x}Zn_xFe_2O_4$ nanoparticles dispersed in a silica matrix by a sol–gel auto-combustion method. Ceram Int 2015;41(January (1)):231–9. Part A.

[13] Abadias G. Stress and preferred orientation in nitride-based PVD coatings. Surf Coat Technol 2008;202:2223–35.

[14] Marulanda Cardona DM, Wongsa-Ngam J, Langdon TG. Microstructural evolution and microhardness in a low carbon steel processed by high-pressure torsion. J Mater Res Technol 2014;3(4):344–8.

[15] Ivanisenko Yu, Lojkowski W, Valiev RZ, Fecht H-J. The mechanism of formation of nanostructure and dissolution of cementite in a pearlitic steel during high pressure torsion. Acta Mater 2003;51(October):5555–70.

[16] Kim JG, Enikeev NA, Abramova MM, Park BH, Valiev RZ, Kim HS. Effect of initial grain size on the microstructure and mechanical properties of high-pressure torsion processed twinning-induced plasticity steels. Mater Sci Eng A 2017;682:164–7.

[17] Pippan R, Scheriau S, Taylor A, Hafok M, Hohenwarter A, Bachmaier A. Saturation of fragmentation during severe plastic deformation. Ann Rev Mater Res 2010;40:319–43.

[18] Larijani N, Kammerhofer C, Ekh M. Simulation of high pressure torsion tests of pearlitic steel. J Mater Process Technol 2015;223(September):337–43.

[19] Kawasaki M, Lee H-J, Ahn B, Zhilyaev AP, Langdon TG. Evolution of hardness in ultrafine-grained metals processed by high-pressure torsion. J Mater Res Technol 2014;3(October–December):311–8.